

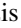



Quasinormal mode theory for multiresonant metasurfaces with superwavelength periodicity involving two-dimensional materials

Thomas Christopoulos ^{1,2,*}, Georgios Nousios ², Emmanouil E. Kriezis ², and Odysseas Tsilipakos ^{1,†}

¹Theoretical and Physical Chemistry Institute, National Hellenic Research Foundation, 11635 Athens, Greece

²School of Electrical and Computer Engineering, Aristotle University of Thessaloniki, 54124 Thessaloniki, Greece



(Received 3 September 2024; revised 17 November 2024; accepted 20 November 2024; published 6 December 2024)

A multimode framework that can be utilized in the analysis and design of metasurfaces with sub- and superwavelength periodicity involving dielectric, plasmonic, or 2D materials is presented. The numerical tool is based on the concept of quasinormal modes (QNMs), which are used to efficiently reconstruct the structure's electromagnetic response. It is general and can be applied to any non-Hermitian periodic resonant system irrespective of pitch value, incidence angle, frequency regime, material composition, and type of supported resonance, including Fabry-Pérot modes, whispering-gallery modes, localized plasmonic resonances and surface states, lattice resonances, dielectric Mie modes, etc. The framework is employed to study two contemporary metasurface structures involving 2D materials: (i) a graphene-based plasmonic metasurface that supports tightly confined surface plasmons which form Fabry-Pérot resonances and (ii) a dielectric metasurface that supports Mie-like resonances and a bound state in the continuum (BIC), enhanced with a transition-metal dichalcogenide bilayer. The ability of supporting sharp resonances through quasidark or qBIC modes as well as the tuning of their resonant frequency via electrical gating are investigated. In each case, the QNMs are retrieved using a modified finite-element scheme that can handle periodic systems with dispersion. They are then fed to the modal framework to specify the spectral response for the zeroth and higher diffraction orders. The results are validated by comparing against time-harmonic finite-element simulations, showing excellent agreement.

DOI: [10.1103/PhysRevB.110.245407](https://doi.org/10.1103/PhysRevB.110.245407)

I. INTRODUCTION

Optical metasurfaces (MSs) have received considerable scientific interest for more than a decade now [1–3], mainly due to their ability to strongly interact with incident radiation despite being electrically thin. They have been used to efficiently control the propagation of light and its properties (direction, polarization, wavefront), mainly in free-space [2,3] but also in guided-wave structures [4]. Towards the goal of efficient and tunable control of light, 2D photonic materials (graphene, transition metal dichalcogenides (TMDs), MXenes, etc.) are being incorporated in MSs for their unique linear and nonlinear properties, which can be additionally externally tuned [5]. Importantly, the infinitesimal thickness of 2D material retains the advantage of an ultrathin composite structure.

The exploding study of metasurfaces and their applications necessitates efficient numerical tools to help with analyzing and designing such contemporary periodic systems. MSs are frequently studied with general-purpose computational methods such as the finite-difference time-domain or the finite-element method (FEM). However, such approaches do not provide the desirable physical intuition needed for probing

the underlying physics and pursuing optimal designs. Additionally, they require significant simulation times, especially when sharp resonances are involved, leading to long energy storage (time domain) or fine frequency resolution to unveil their narrow linewidths (frequency domain). On the contrary, *modal* techniques aim to examine light-matter interaction at its core, focusing on the pole structure of the system under study and allowing for physics-informed designs that efficiently exploit the supported resonances [6–8]. In many instances, having a clear view of the supported resonances has proven quite useful in the design of resonant systems [6,9–11]. However, developing such modal techniques in contemporary photonic systems with loss, dispersion, and significant radiation damping (leakage) is not a trivial task.

Here, we contribute toward this direction by presenting a modal framework for resonant metasurfaces with *superwavelength* periodicity that is based on quasinormal modes (QNMs), i.e., the modes that are supported by non-Hermitian systems. The framework allows for the treatment of any general periodic resonant photonic system, irrespective of the frequency regime (visible, near infrared, THz, microwaves), material composition (dielectrics, metals, 2D materials), or type of supported resonance, be it plasmonic (i.e., bound to a surface or interface), Fabry-Pérot (FP), Mie, bound states in the continuum, or other. The accuracy (compared with other simulation methods or even experiments) and efficiency (in terms of speed reduction) of QNM-based techniques [12,13] has been already proven in guided-wave systems [14], plasmonic nanoparticles [15], and

*Present address: Laboratoire Photonique, Numérique et Nanosciences (LP2N), IOGS-University of Bordeaux-CNRS, 33400 Talence, France; Contact author: cthomasa@eie.gr

†Contact author: otsilipakos@eie.gr

metasurfaces (subwavelength pitch) with plasmonic [10] and 2D materials [9].

In this paper, we showcase how the developed QNM framework can be used to study metasurfaces with superwavelength pitch through two examples that involve the entire gamut of plasmonic, photonic, and Mie resonances. Combining the resonant scatterers of metasurfaces with the superwavelength periodicity of gratings can lead to even richer phenomena, since higher diffraction orders (DOs) allow for further control of light by opening different propagation channels. This may lead to advanced linear, nonlinear, or quantum applications [16]. The examples are carefully selected to refer to contemporary concepts such as dark modes and (quasi)bound states in the continuum (BICs and qBICs) [3,17,18] in systems that are capable of electrical tunability and advanced functionalities (e.g., nonlinear response and light emission). Specifically, we apply the proposed framework in a graphene-based MS which supports plasmonic modes, and in a dielectric (silicon-rich nitride) MS, enhanced with a transition-metal dichalcogenide bilayer, which supports Mie-like modes and a BIC. The selected 2D materials can be tuned electrically, they are highly nonlinear, and they exhibit the ability for light amplification and emission. Due to the superwavelength pitch, higher diffraction orders become propagating for different wavelengths or incidence angles. In both cases, the spectral response is reconstructed by the QNM framework for each diffraction order and compared against full-wave FEM time-harmonic simulations, showing excellent agreement. Time-harmonic FEM simulations were chosen for the verification process, as the same mesh can be used to ensure a fair comparison between the two approaches. To minimize sources of possible numerical error, we have taken care to allow for a sufficiently dense discretization (verified by the convergence of the time-harmonic FEM results), retain a sufficient number of terms in the QNMs framework (verified by gradually incorporating additional modes and checking the convergence), and use robust boundary conditions (perfectly matched layers) for the truncation of the computational domain. Note that agreement in the numerical results of QNM frameworks with other computational methods, including the FEM, have been also reported in the literature [12].

The rest of the paper is organized as follows. In Sec. II, we build upon mature concepts and present the aspects of the proposed QNM framework, i.e., the treatment of periodic systems with 2D materials and higher DOs. In Sec. III, we focus on the analysis of a graphene-based MS that mainly supports plasmonic modes, while in Sec. IV we examine a dielectric system that supports Mie-like resonances and a BIC.

We calculate the spectral response of these two MSs and also investigate, interpret, and discuss interesting features that they exhibit. Finally, Sec. V provides concluding remarks.

II. QNM FRAMEWORK FOR PERIODIC SYSTEMS WITH PROPAGATING DIFFRACTION ORDERS

It is commonly accepted that the QNMs, $\tilde{\mathbf{E}}_m(\mathbf{r})$, supported by a non-Hermitian cavity form an orthonormal basis that can be used to decompose the scattered field $\mathbf{E}_{\text{sct}}(\mathbf{r}, \omega)$ through

$$\mathbf{E}_{\text{sct}}(\mathbf{r}, \omega) = \sum_m a_m(\omega) \tilde{\mathbf{E}}_m(\mathbf{r}), \quad (1)$$

where $a_m(\omega)$ are expansion coefficients that depend on the resonator (materials, geometry) and the form of the excitation [6]. The tilde symbol in this paper is reserved to denote modal quantities (eigenvectors, i.e., QNMs, and their respective eigenvalues, i.e., complex resonance frequencies). Equation (1) is accurate (complete) when all QNMs are considered [19]. This cannot be strictly accomplished, but Eq. (1) can still hold quite accurately, particularly when nonphysical modes that emerge in the frequency range of interest due to the truncation of the computational space with open boundary conditions [20] or perfectly matched layers (PMLs) [15] are additionally included.

In periodic systems, one typically examines a single unit cell by utilizing the Bloch-Floquet theorem which states that the total electric field $\mathbf{E}(\mathbf{r})$ is periodic [21,22], i.e., $\mathbf{E}(\mathbf{r}) = \mathbf{e}(\mathbf{r}) \exp\{-jk_0 \boldsymbol{\eta} \cdot \mathbf{r}_{\parallel}\}$, where k_0 is the free-space wave number, $\boldsymbol{\eta}$ is extracted from the Floquet wave vector as $\mathbf{k}_F = k_0 \boldsymbol{\eta}$, and $\mathbf{e}(\mathbf{r})$ is the periodic electric field envelope. Then, Eq. (1) is expressed as

$$\mathbf{E}_{\text{sct}}(\mathbf{r}, \omega) = \sum_m a_m(\omega) \tilde{\mathbf{e}}_m(\mathbf{r}) \exp\{-j\tilde{k}_m \boldsymbol{\eta} \cdot \mathbf{r}_{\parallel}\}, \quad (2)$$

which involves only the spatial envelope of the QNMs and their (complex) wave numbers $\tilde{k}_m = \tilde{\omega}_m/c_0$. The envelopes $\tilde{\mathbf{e}}_m(\mathbf{r})$ can be retrieved with a FEM eigenvalue solver. However, to correctly model oblique incidence in periodic structures, one has to use a modified Helmholtz equation, expressed in terms of the spatial envelope, $\mathbf{e}(\mathbf{r})$, rather than the full field, $\mathbf{E}(\mathbf{r})$. Although nontrivial, this process is well established in the literature [9,10,23,24] (sometimes referred to as ω - γ formulation [24]) and it is utilized in this work. In addition, we need to carefully normalize the spatial envelopes of the QNMs [6,9,10,13,15]. Specifically, starting from the biorthogonality condition for the spatial envelopes of the QNMs [9,10], one can show that $\tilde{\mathbf{e}}_m(\mathbf{r})$ and $\tilde{\mathbf{h}}_m(\mathbf{r})$ should be normalized as

$$\iiint_V \left[\tilde{\mathbf{e}}_{-m} \cdot \frac{\partial\{\omega\varepsilon\}}{\partial\omega} \tilde{\mathbf{e}}_m - \tilde{\mathbf{h}}_{-m} \cdot \frac{\partial\{\omega\mu\}}{\partial\omega} \tilde{\mathbf{h}}_m - \tilde{\mathbf{e}}_{-m} \cdot j \frac{\partial\sigma_s}{\partial\omega} \tilde{\mathbf{e}}_m \delta_s - \boldsymbol{\eta} \cdot \frac{1}{c_0} (\tilde{\mathbf{h}}_{-m} \times \tilde{\mathbf{e}}_m + \tilde{\mathbf{e}}_{-m} \times \tilde{\mathbf{h}}_m) \right] dV = 1, \quad (3)$$

where $\tilde{\mathbf{e}}_{-m}$ and $\tilde{\mathbf{h}}_{-m}$ denote left eigenvectors (left QNMs), which are necessary to ensure biorthogonality [10,19,25], and $\delta_s(\mathbf{r} - \mathbf{r}_0)$ is a surface Dirac function, nonzero only on the 2D material surface denoted by \mathbf{r}_0 . For the rest of the paper, all QNMs are considered as having been normalized via Eq. (3).

Note that we use the so-called PML normalization, i.e., we truncate the computational domain via PMLs and perform the integration of Eq. (3) inside the artificial domains as well [26]. Finally, the derivatives of $\varepsilon(\omega)$, $\mu(\omega)$, and $\sigma_s(\omega)$ are evaluated at the complex frequency $\omega = \tilde{\omega}_m$.

Depending on the involved materials (bulk or sheet, with or without dispersion) and the excitation type (point dipole, plane wave, etc.), the expansion coefficients $a_m(\omega)$ acquire different expressions [9,10,15,26]. Here, we will consider both bulk and sheet materials with multipole Drude-Lorentz dispersion and plane-wave illumination. In Ref. [9], a similar equation is presented but for a single scatterer. In the same work, it was discussed how the expansion coefficients emerge from the scattering form of the curl Maxwell equations, utilizing the expansion of Eq. (1) and biorthogonality. Here, we give its equivalent for a periodic system

$$a_m(\omega) = \frac{1}{\tilde{\omega}_m - \omega} \iiint_V [\tilde{\mathbf{e}}_{-m} \cdot \omega \varepsilon_0 (\varepsilon_\infty - \varepsilon_b) \mathbf{e}_b + \tilde{\mathbf{e}}_{-m} \cdot \tilde{\omega}_m \varepsilon_0 (\varepsilon_r(\tilde{\omega}_m) - \varepsilon_\infty) \mathbf{e}_b + \tilde{\mathbf{e}}_{-m} \cdot j\sigma_s(\tilde{\omega}_m) \mathbf{e}_b \delta_s] dV, \quad (4)$$

where we have used the general dispersion expressions

$$\varepsilon_r(\omega) = \varepsilon_\infty \left(1 - \sum_{i=1}^N \frac{\omega_{p,i}^2}{\omega^2 - \omega_{0,i}^2 - j\omega\gamma_i} \right), \quad (5a)$$

$$\sigma_s(\omega) = -j\omega\varepsilon_0 \sum_{i=1}^N \frac{\omega_{p,i}^2}{\omega^2 - \omega_{0,i}^2 - j\omega\gamma_i}, \quad (5b)$$

for bulk and sheet materials, respectively. In Eq. (4), we denote with $\mathbf{e}_b(\mathbf{r})$ the spatial envelope of the background field, i.e., the field in the absence of the cavity consisting of the incident field, $\mathbf{e}_{\text{in}}(\mathbf{r})$, plus the reflected field, $\mathbf{e}_r(\mathbf{r})$, from the substrate (if any), so $\mathbf{e}_b(\mathbf{r}) = \mathbf{e}_{\text{in}}(\mathbf{r}) + \mathbf{e}_r(\mathbf{r})$.

To calculate the response of the MS, we need the *total* full field, i.e., $\mathbf{E}_{\text{tot}}(\mathbf{r}) = \mathbf{E}_{\text{sct}}(\mathbf{r}) + \mathbf{E}_b(\mathbf{r})$. Then, it is straightforward to calculate the absorbed power as

$$P_{\text{abs}} = \frac{1}{2} \iiint_V \text{Re}\{j\omega\varepsilon_0(\varepsilon_r - 1) + \sigma_s\delta_s\} \mathbf{E}_{\text{tot}} \cdot \mathbf{E}_{\text{tot}}^* dV, \quad (6)$$

with the integration taking place inside the cavity. To calculate the reflection and/or transmission coefficients, we need the reflected and transmitted wave *outside* the cavity, which may be obtained through Eq. (2). Although the QNM expansion is not strictly complete outside the cavity [19], Eq. (2) can still be used and this approach has been shown to give very good results [9,10].

Besides specular reflection and transmission in periodic metasurfaces with subwavelength pitch, the proposed framework can capture higher diffraction orders that become propagating in resonant metasurfaces with superwavelength pitch. Let us assume the general case of an MS that is periodic along the x and y directions. The MS is illuminated from the top by an oblique plane wave with angles of incidence ϑ_i (polar angle) and ϕ_i (azimuthal angle). Then, the wave vector of the incident wave is $\mathbf{k}_i = k_0 n_1 (\sin \vartheta_i \cos \phi_i \hat{\mathbf{x}} + \sin \vartheta_i \sin \phi_i \hat{\mathbf{y}} - \cos \vartheta_i \hat{\mathbf{z}}) = \alpha_0 \hat{\mathbf{x}} + \beta_0 \hat{\mathbf{y}} + \gamma_0 \hat{\mathbf{z}}$, and $\boldsymbol{\eta} = n_1 (\sin \vartheta_i \cos \phi_i \hat{\mathbf{x}} + \sin \vartheta_i \sin \phi_i \hat{\mathbf{y}})$. Now, denoting with Λ_x and Λ_y the pitch (lattice constant) across the x and y directions, respectively, the parallel-to-the-metasurface wave-vector components are $\alpha_m = \alpha_0 + m(2\pi/\Lambda_x)$, $\beta_n = \beta_0 + n(2\pi/\Lambda_y)$ for any

diffraction channel of order (m, n) . This DO becomes propagating when the normal component of the wave vector $\gamma_{mn} = \pm [(k_0 n_i)^2 - \alpha_m^2 - \beta_n^2]^{1/2}$ is real, i.e., for $(k_0 n_i)^2 > \alpha_m^2 + \beta_n^2$; here $i = \{1, 2\}$, referring to the side of the incidence or transmission, respectively, and the plus (minus) sign is used as well for the reflected (transmitted) wave.

Next, let us assume a fictitious plane at $z = \pm d$. Only the components of the scattered electric field that lie on this plane, $\mathbf{E}_{\text{sct}}^t(x, y, d)$, are necessary for the subsequent calculations (t stands for tangential). We expand them in 2D Fourier series (Rayleigh expansion) and find that the respective amplitudes are

$$E_{k,\text{sct},mn} = \frac{1}{\Lambda_x \Lambda_y} \iint_S E_{k,\text{sct}}(x, y, d) e^{j(\alpha_m x + \beta_n y)} dx dy, \quad (7)$$

with $k = \{x, y\}$ and S the surface of the unit cell. For calculating reflection and transmission to the different diffraction orders, it is more convenient to use the scattered field in p (parallel) and s (normal) polarization. Having calculated the x and y components of the scattered field and making use of the angles $\vartheta_{mn} = \cos^{-1}(\pm \gamma_{mn}/k_0 n_i)$, $\phi_{mn} = \tan^{-1}(\beta_m/\alpha_n)$, with ϑ_{mn} measured from the positive z -axis direction to the tip of the wave vector and the plus (minus) sign corresponding to the reflected (transmitted) wave, we can write

$$E_{p,\text{sct},mn} = \frac{\cos \phi_{mn} E_{x,\text{sct},mn} + \sin \phi_{mn} E_{y,\text{sct},mn}}{\cos \vartheta_{mn}}, \quad (8a)$$

$$E_{s,\text{sct},mn} = \sin \phi_{mn} E_{x,\text{sct},mn} - \cos \phi_{mn} E_{y,\text{sct},mn}, \quad (8b)$$

respectively. To obtain the amplitude reflection r_{mn} and transmission t_{mn} coefficients, each output polarization should be associated with the respective input polarization unless cross-polarization effects are expected. Finally, for the zeroth diffraction order $m = n = 0$, note that background reflection and transmission in the absence of the cavity should be first added to the scattered field to calculate the respective reflection and transmission coefficients. For example and for a single polarization (p - p or s - s), power transmission coefficients can be calculated as $|t_0|^2 = |t_{\text{bg}} + E_{\text{sct},0}/E_{\text{in}}|^2 (n_2/n_1)$ for $m = n = 0$ and $|t_{mn}|^2 = |E_{\text{sct},mn}/E_{\text{in}}|^2 (n_2/n_1) (\cos \vartheta_{mn}/\cos \vartheta_i)$ for $m, n \neq 0$. Similar expressions stand for power reflection coefficients.

III. GRAPHENE METASURFACE WITH PLASMONIC FABRY PÉROT RESONANCES

As a first example, we will examine an MS consisting of periodically arranged graphene strips lying on a metal-backed glass substrate [9,27,28], as shown in Fig. 1. We will focus on THz frequencies where graphene supports tightly confined graphene surface plasmons (GSPs) owing to the Drude-like dispersion of its surface conductivity $\sigma_s(\omega) = -j\sigma_0/(\omega - j\gamma_{\text{gr}})$. Assuming incidence within the xz plane, GSPs which are necessarily TM polarized ($\mathbf{H} \parallel \hat{\mathbf{y}}$) will propagate along the $\pm x$ axis and form horizontal FP resonances because of reflection at the graphene edges [9,29]. Due to its uniformity along the y axis, we can study the system as a 2D structure. We will simulate a single unit cell with the boundary conditions shown in Fig. 1(b). The dimensions are provided in the caption. For this pitch value, higher DOs

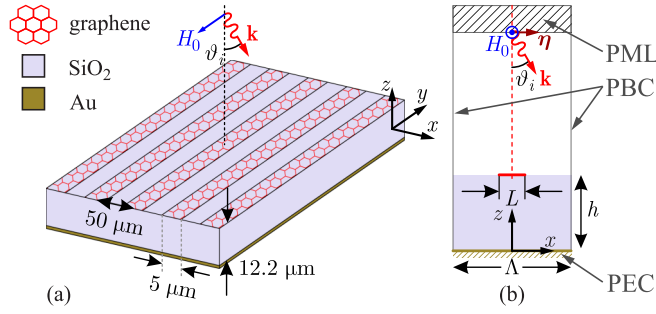


FIG. 1. (a) 3D schematic of the considered MS, with periodically arranged graphene strips laying on a metal-backed glass substrate. FP resonances in the low THz band appear due to the supported GSPs that propagate along the x axis. (b) 2D equivalent unit cell that is used for the simulations. The geometric parameters of the MS are $L = 5 \mu\text{m}$, $\Lambda = 50 \mu\text{m}$, and $h = 12.2 \mu\text{m}$. The material properties are $n_{\text{inc}} = 1$, $n_{\text{sub}} = 1.45$, and $\sigma_0 = 35.3 \text{ mS/ps}$ ($\mu_c = 0.3 \text{ eV}$), $\gamma_{\text{gr}} = 0.025 \text{ Trad/s}$ for graphene. The applied boundary conditions are also shown in the schematic.

will become propagating in the frequency range of interest (3–6.5 THz) as the incidence angle increases.

We will calculate the response of the examined MS using the developed framework. To find the QNMs under oblique incidence, we solve a modified Helmholtz equation that uses the periodicity vector $\eta = n_{\text{inc}} \sin \vartheta_i \hat{x}$, complemented with an additional equation involving an auxiliary field to capture graphene dispersion [9]. In Fig. 2(a), we show in the complex plane some of the obtained modes in the range 3–6.5 THz, assuming $\vartheta_i = 60^\circ$. We find not only FP plasmonic modes (X markers) but also other modes that are located mostly in the dielectrics (O markers) and spurious modes (Δ markers) that represent the branch cuts which appear when a DO becomes propagating. The distribution of the \tilde{e}_x component is included in Fig. 2(a) in some characteristic cases. These QNMs, along with additional spurious modes (approximately 400), are used to apply the proposed framework. Note that this large number of modes is needed to obtain a perfect reconstruction of the full-wave solution [10,13]; the spectral features are already qualitatively reproduced by including the few modes of physical origin that are predominantly involved in the process. Absorption and reflection are shown with red thick solid lines in Figs. 2(b) and 2(c), respectively, and are compared with time-harmonic FEM simulations (blue dots), showing excellent agreement. Note that this excellent reconstruction is observed even for reflection, although, as stated, the QNM expansion is not strictly complete outside the cavity. Interestingly, both absorption and reflection are very low in the spectral vicinity of the TM_1 mode. Most of the incident power in this case is redirected toward the $\ell = -1$ DO, i.e., toward $\vartheta_{r,-1} = -49^\circ$, instead of $\vartheta_{r,0} = 60^\circ$ of the specular direction. This is seen in Fig. 2(d), where the r_{-1} coefficient is plotted. This is a very interesting result that is validated by the full-wave solution, indicating how the examined MS can be used for, e.g., anomalous beam steering applications.

Next, the incidence angle is varied to 40° and 0 . For each case, the frequency above which the lowest order DO ($\ell = -1$) becomes propagating is clearly marked in Fig. 2 and

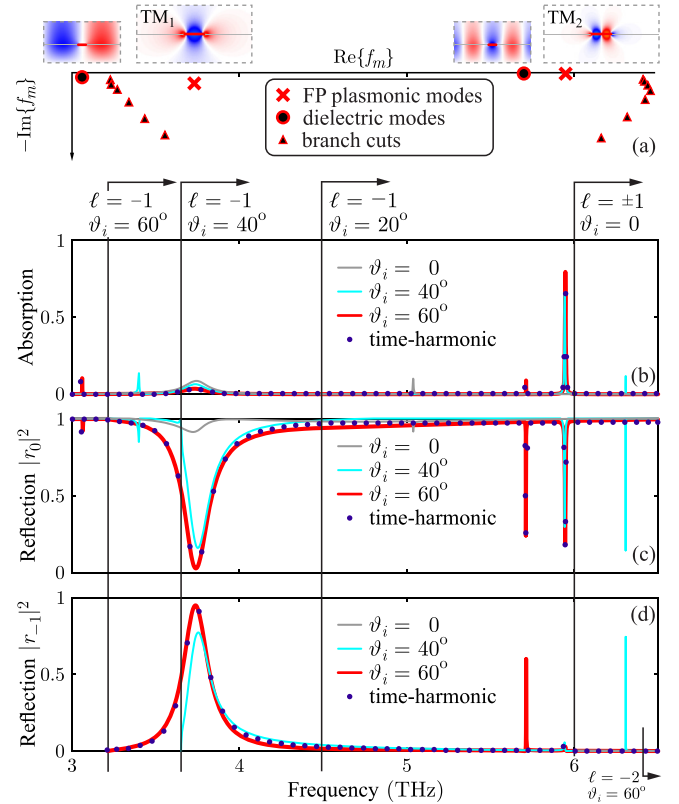


FIG. 2. (a) Pole structure of the MS for oblique incidence ($\vartheta_i = 60^\circ$). The field distribution (\tilde{e}_x component) for a few characteristic QNMs is also included in insets. (b) Absorption and (c) specular reflection for normal and oblique incidence. As ϑ_i deviates from 0, the resonance frequency of the symmetric TM_1 graphene FP resonance remains practically constant, but the radiation quality factor changes considerably. The antisymmetric TM_2 FP resonance is only excited for $\vartheta_i \neq 0$. For $\vartheta_i \sim 60^\circ$, specular reflection in the spectral vicinity of the TM_1 mode practically vanishes. (d) Reflection of the $\ell = -1$ DO. For $\vartheta_i = 60^\circ$, the incident light is almost completely diverted towards the $\ell = -1$ propagating DO ($\vartheta_{r,-1} = -49^\circ$). All absorption and reflection curves are calculated using the QNM framework and validated for $\vartheta_i = 60^\circ$ through time-harmonic plane-wave-scattering FEM simulations.

corresponds to [30]

$$\lambda_{\ell, \text{cutoff}} = n_{\text{inc}} (1 \mp \sin \vartheta_i) \frac{\Lambda}{|\ell|}. \quad (9)$$

Equation (9) is valid for both positive and negative indices ℓ . We see that the resonance frequencies of the two FP plasmonic modes remain practically unaffected and only the respective Q factors are different, as indicated by the peaks (dips) in absorption (specular reflection) spectrum. Dielectric modes, on the other hand, shift quite significantly with ϑ_i , since the effective length that light travels inside the substrate is $\propto 1/\cos \vartheta_i$. Furthermore, note that the TM_2 mode cannot be excited under normal E_x -polarized incidence (dark mode), since the distribution of the \tilde{e}_x component is antisymmetric [inset in Fig. 2(a)]. This is reflected in $Q_{\text{rad}} \rightarrow \infty$ and is nowadays commonly referred to as a symmetry-protected BIC [3]. As ϑ_i deviates from 0, the TM_2 mode is also excited by the incident TM wave. However, there are some additional incident

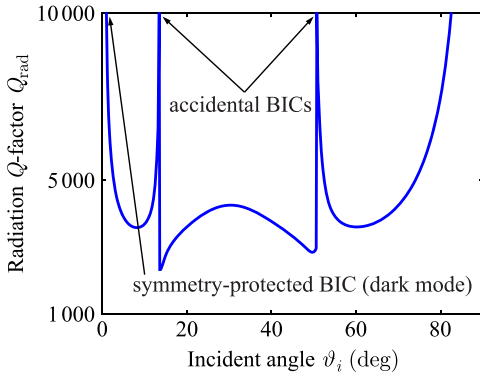


FIG. 3. Radiation quality factor (Q_{rad}) of the TM_2 mode as a function of the incident angle ϑ_i . For $\vartheta_i = 0$, there exists a symmetry-protected BIC (dark mode) with infinite Q factor. There are also accidental BICs that emerge due to destructive interference in reflection.

angle values at which Q_{rad} diverges to practically infinite values. In Fig. 3, we plot Q_{rad} for the TM_2 mode as a function of ϑ_i . For angles 13.4° and 50.8° , Q_{rad} diverges and the TM_2 mode cannot be excited. This is not anticipated by symmetry arguments; rather, it arises due to destructive interference in the reflected wave which gives rise to accidental BICs [3,31].

Finally, we will demonstrate the tuning capabilities enabled by graphene. By applying an external bias between graphene and the metal back-plane, we can electrically tune the surface conductivity of the former by modifying its Fermi level ($\sigma_0 \propto \mu_c$). In effect, this strongly affects the resonant frequencies and quality factors of the GSP resonances. We focus on $\vartheta_i = 60^\circ$ and consider moderate values for μ_c in the range 0.3–0.4 eV. The results are depicted in Fig. 4. Specifically, in Figs. 4(a) and 4(b), we include the total quality factor (Q_{tot}), the radiation quality factor (Q_{rad}), and the resonance frequency (f_0) of the TM_1 and TM_2 modes as a function of μ_c . We find a linear blueshift for f_0 and a suppression of the quality factor due to the additional radiation for larger μ_c values. For the TM_2 mode, the change in μ_c shifts its resonance frequency above the propagation limit of the $\ell = -2$ DO, highlighted using dashed lines in Fig. 4(b). When this happens, the radiation behavior of the mode changes, leading to a significant suppression of the respective Q factor [see the characteristic “knee” in Fig. 4(b)]. Tuning of the resonant frequencies and Q s is also seen in the reflection spectra depicted in Figs. 4(c) and 4(d) for the fundamental and higher DOs, respectively (note that the $\ell = -2$ DO becomes propagating for $f > 6.45$ THz and a significant part of TM_2 reflection is toward that DO). On the contrary, dielectric modes are only marginally affected since they mostly lie on the substrate (see the resonance around 5.7 THz).

IV. DIELECTRIC METASURFACE WITH A MIE-LIKE BIC RESONANCE

As a second example, we will examine a dielectric metasurface in the near infrared. The considered periodic system is depicted in Fig. 5. It consists of dielectric [silicon-rich silicon nitride (SRN)] meta-atoms (wires) lying on a glass substrate.

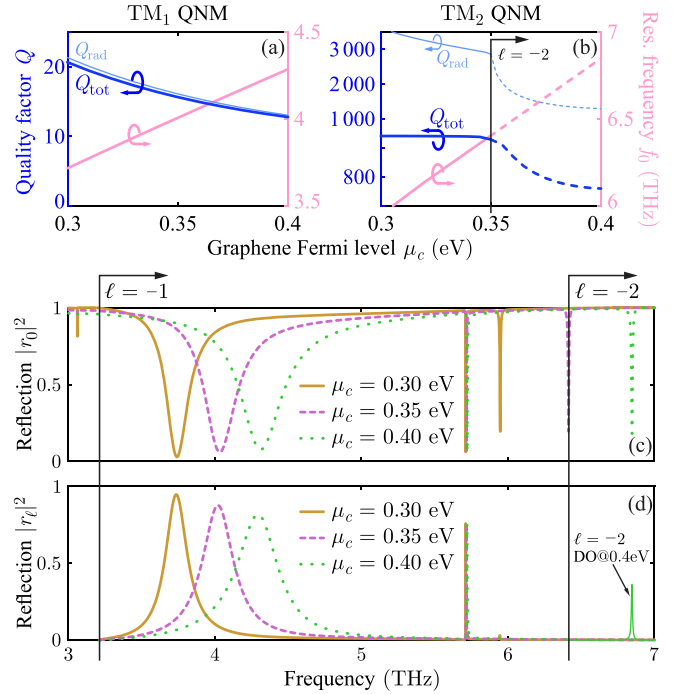


FIG. 4. Total quality factor, (Q_{tot}) radiation quality factor (Q_{rad}), and resonance frequency of (a) TM_1 and (b) TM_2 modes with respect to the Fermi level of graphene for $\vartheta_i = 60^\circ$. Both modes experience a linear blueshift as μ_c increases. The respective total Q factor is restricted due to the additional radiation for larger μ_c values. This is more evident in the TM_2 QNM, where also a different radiation behavior leads to a strong decrease in Q when the $\ell = -2$ DO becomes propagating (notice the characteristic “knee”). (c) Specular reflection and (d) reflection towards higher DOs. The findings of (a) and (b) are clearly observable in the shown spectrum.

This time, no metal backing is present, thus allowing for both reflection and transmission through the metasurface. This MS supports Mie-like resonances in the SRN meta-atoms and it is enhanced with a TMD heterobilayer on top to allow for additional functionality, such as second-order nonlinear effects

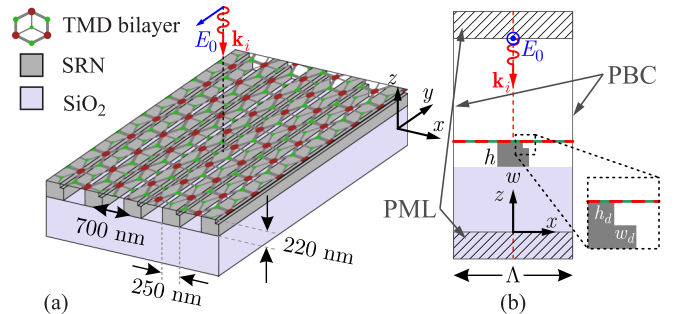


FIG. 5. (a) 3D schematic of the considered SRN wire metasurface, enhanced with a TMD bilayer on top. A defect is introduced on the top-right corner to allow for the excitation of a Mie-like qBIC mode. (b) 2D equivalent unit cell that is used for the simulations. The geometric parameters of the MS are $w \times h = 250 \text{ nm} \times 220 \text{ nm}$, $w_d = h_d = 30 \text{ nm}$ (unless mentioned otherwise), and $\Lambda = 700 \text{ nm}$. The background material properties are $n_{\text{inc}} = 1$ and $n_{\text{sub}} = 1.45$. The applied boundary conditions are also shown in the schematic.

TABLE I. Values used for simulations in the Drude-Lorentz models for SRN and TMD bilayer.

	ϵ_∞	N	ω_p (Trad/s)	ω_0 (Trad/s)	γ (Trad/s)
SRN	1	1	15 740	5 529	2
			2.239	14 270	
TMD	1	3	0.0127	1 670	20
			0.0775	2 546	70

[32,33], external tunability [34], or light emission [35]. The geometric parameters are provided in the caption of Fig. 5. Given the pitch of $\Lambda = 700$ nm and the frequency range of interest $\lambda_0 = 600$ –1200 nm, higher DOs will become propagating in this case as well. We examine TE polarization ($\mathbf{E} \parallel \hat{\mathbf{y}}$) and focus on normal incidence. Importantly, we will demonstrate how a BIC that is supported by the MS can be excited by introducing a geometric asymmetry [see the inset of Fig. 5(b)] rather than an asymmetry in the excitation (e.g., oblique incidence), as exercised in Sec. III. Regarding the electromagnetic properties of SRN and the TMD bilayer, we assume that both are described by Drude-Lorentz functions [Eqs. (5)] to correctly capture their dispersion. In Table I, we compile the parameters used to model SRN and the TMD bilayer [34,36–38].

We simulate a unit cell of the considered dielectric MS and solve for the supported modes (physical and spurious). We examine an octave-spanning frequency window from 600 nm to 1200 nm and depict in Fig. 6(a) some of these modes, namely, Mie-like modes (X markers), spurious modes (Δ markers) that represent branch cuts, and also numerous plasmonic modes (O markers) that accumulate at 740 nm and 1128 nm, respectively; this is a well-reported effect close to a Drude-Lorentz pole [39]. Omitting the plasmonic modes when reconstructing the spectral response can have a non-negligible impact, but mostly in the absorption curve. Using the depicted modes, as well as additional spurious (PML) modes (approximately 600), we apply the proposed framework and plot in Figs. 6(b)–6(d) absorption, reflection, and transmission, respectively. We examine scenarios with (red thick lines) and without (gray thin lines) a geometric defect consisting of a 30×30 nm² indentation in the upper right corner of the SRN meta-atom. Time-harmonic FEM simulations (blue markers) are used to verify the red curves (case with defect). As expected, the small defect does not significantly affect the response of the MS in most of the spectrum. However, it allows for the excitation of the qBIC mode at 1160 nm, resulting in a sharp Fano-like line shape, due to interference with additional reflection channels [40].

To further highlight the excitation of the qBIC resonance, we plot Q_{rad} as a function of the defect size in Fig. 7. The initially infinite radiation Q factor drops to a few thousands. The purely vertical magnetic dipole moment (m_z) exhibited by the TE₂ mode acquires a horizontal (m_x) component that allows radiation leakage toward the $\pm z$ direction. In the inset, the evolution of the Fano line shape with increasing defect size is depicted. There is a notable change (blueshift) of the qBIC resonance frequency and, importantly, in the linewidth.

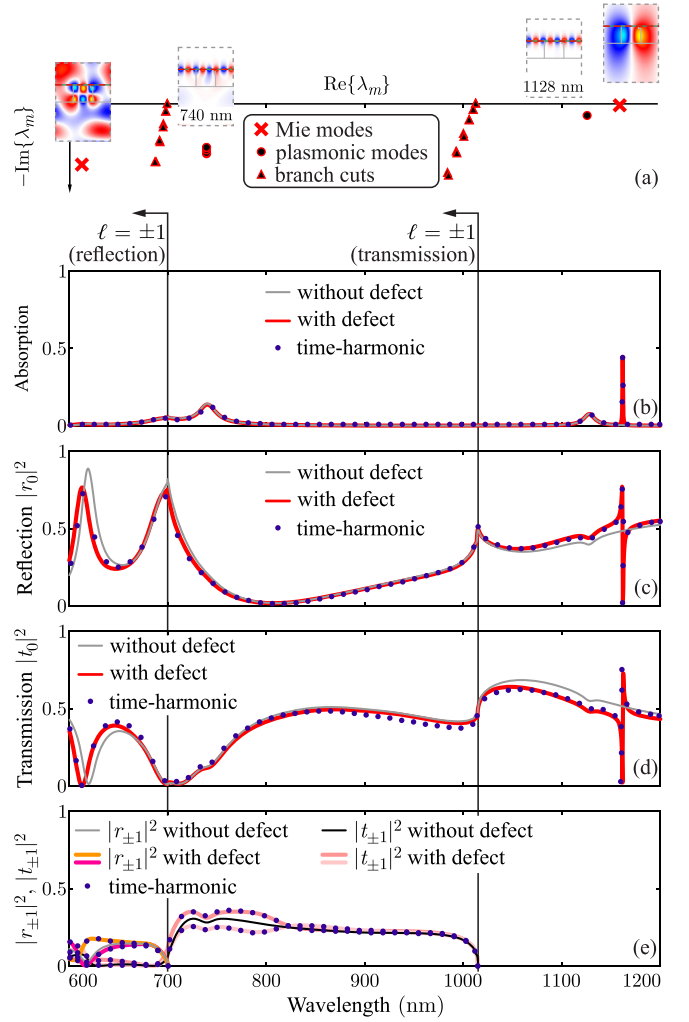


FIG. 6. (a) Pole structure of the MS with the geometric defect for normal incidence. Two Mie-like resonances, numerous plasmonic modes, and two branch cuts can be identified. The field distribution (\vec{e}_y component) of a few indicative modes is also included. (b) Absorption, (c) reflection, and (d) transmission of the MS (normal, TE-polarized incidence) with or without the defect. The (q)BIC around 1160 nm can be only excited when the defect is introduced (a horizontal, m_x , magnetic dipole component develops). (e) Reflection and transmission of the $\ell = \pm 1$ DOs. In the absence of the defect, light is symmetrically diffracted whereas the presence of the defect breaks this symmetry. All absorption, reflection, and transmission curves are calculated using the QNM framework and are validated for the defect case by comparing against time-harmonic plane-wave-scattering FEM simulations (dot markers).

The spectral feature becomes broader and stronger as Q_{rad} decreases.

We also use Eq. (7) to calculate reflection and transmission to higher DOs [Fig. 6(e)]. Because of the normal incidence, $\ell = \pm 1$ DOs become propagating at the same wavelength and, in the absence of a defect, they both have the same efficiency (carry the same power). This is depicted in Fig. 6(e) (gray and black lines). Note, however, that since $n_{\text{sub}} > n_{\text{inc}}$, transmission DOs appear first (for $\lambda < 1015$ nm) and reflection DOs follow (for $\lambda < 700$ nm). On the other hand, for the case with

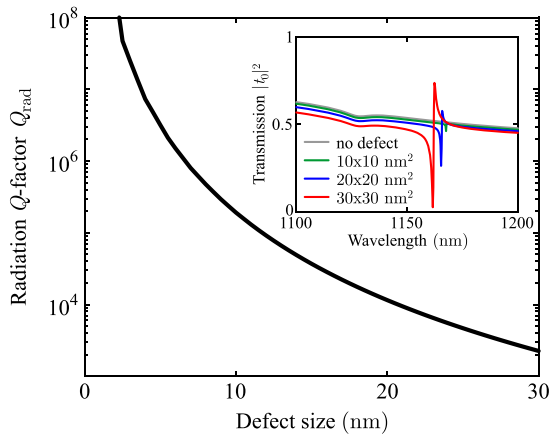


FIG. 7. Radiation quality factor (Q_{rad}) of the (q)BIC Mie mode as a function of the defect size. Due to the defect, the TE_2 mode acquires an m_x component in the magnetic dipole moment, allowing interaction with normally-incident plane waves. This translates into finite Q_{rad} values; larger defects allow for stronger coupling. Inset: Spectral response in the vicinity of the (q)BIC resonance for different defect sizes. A larger defect is associated with a wider linewidth due to the lower Q_{rad} value.

defects, it is expected that each transmission and reflection DO will feature a slightly different efficiency (carry a different power fraction) due to the geometric asymmetry of the SRN wire. This is indeed verified in Fig. 6(e), both using the QNMs framework and full-wave FEM simulations.

Finally, we note that the electromagnetic properties of the TMD heterobilayer can be electrically tuned by utilizing the Stark effect [34], i.e., a shifting of the energy band to change the respective band gap via the application of a small static bias. Equivalently, this means that ω_0 in the Drude-Lorentz model [Eq. (5)] can be externally controlled, shifting the location of a Drude-Lorentz pole. For the response of the system, such an action mainly shifts the respective absorption peak and only marginally modifies reflection and transmission. This can be quite interesting in cases where one tries to align the energy band gap of the TMD with the qBIC resonance frequency and enhance, for example, stimulated (lasing) or

spontaneous (Purcell enhancement) emission. Likewise, the sharp line shape of the qBIC mode can be utilized to enhance nonlinear effects, such as second-harmonic generation [32,33] (TMDs are not centrosymmetric materials and favor second-order nonlinearities [41]).

V. CONCLUSION

In conclusion, we have presented and evaluated a modal framework that allows for the efficient and accurate analysis of metasurfaces with superwavelength periodicity, capable of calculating reflection and transmission in specular and higher propagating diffraction orders as well as absorption. The framework requires the calculation of the QNMs supported by the non-Hermitian resonant system through a single eigenvalue simulation of the unit cell and, following an appropriate normalization, uses these eigenmodes as a basis to expand the scattered field. It is, thus, very efficient and also very accurate, as proven by comparing against full-wave time-harmonic simulations.

The capabilities of the framework have been showcased by two judiciously selected examples: (i) a graphene-based metasurface supporting plasmonic Fabry-Pérot resonances at THz frequencies and (ii) a dielectric metasurface supporting Mie-type resonances at near-infrared frequencies. The ability of supporting sharp resonances through quasdipole or qBIC modes and the tuning of their resonant frequency via electrical gating have been investigated. More generally, the presented framework can be used to study any periodic resonant system irrespective of pitch value, frequency regime, material composition, and type of supported resonance. It can, thus, prove very useful in the analysis and design of modern photonic structures.

ACKNOWLEDGMENTS

This research work was supported by the Hellenic Foundation for Research and Innovation (H.F.R.I.) under the 2nd Call for H.F.R.I. Research Projects to Support Post-Doctoral Researchers (Project No. 916, PHOTOSURF). The authors thank P. Lalanne for his comments during the revision of the paper.

-
- [1] C.-W. Qiu, T. Zhang, G. Hu, and Y. Kivshar, Quo vadis, metasurfaces? *Nano Lett.* **21**, 5461 (2021).
 - [2] O. A. M. Abdelaouf, Z. Wang, H. Liu, Z. Dong, Q. Wang, M. Ye, X. R. Wang, Q. J. Wang, and H. Liu, Recent advances in tunable metasurfaces: Materials, design, and applications, *ACS Nano* **16**, 13339 (2022).
 - [3] D. C. Zografopoulos and O. Tsilipakos, Recent advances in strongly resonant and gradient all-dielectric metasurfaces, *Mater. Adv.* **4**, 11 (2023).
 - [4] O. Tsilipakos and T. Koschny, Shaping the profile and dispersion of waves guided between spatiotemporally dispersive, electrically and magnetically conductive metasurface boundaries, *IEEE Trans. Antennas Propag.* **72**, 6472 (2024).
 - [5] M. Esfandiari, A. Lalbakhsh, P. Nasiri Shehni, S. Jarchi, M. Ghaffari-Miab, H. Noori Mahtaj, S. Reisenfeld, M. Alibakhshikenari, S. Koziel, and S. Szczepanski, Recent and emerging applications of graphene-based metamaterials in electromagnetics, *Mater. Des.* **221**, 110920 (2022).
 - [6] P. Lalanne, W. Yan, K. Vynck, C. Sauvan, and J. P. Hugonin, Light interaction with photonic and plasmonic resonances, *Laser Photonics Rev.* **12**, 1700113 (2018).
 - [7] P. T. Kristensen, K. Herrmann, F. Intravaia, and K. Busch, Modeling electromagnetic resonators using quasinormal modes, *Adv. Opt. Photonics* **12**, 612 (2020).
 - [8] L. Huang, L. Xu, D. A. Powell, W. J. Padilla, and A. E. Miroshnichenko, Resonant leaky modes in all-dielectric metasystems: Fundamentals and applications, *Phys. Rep.* **1008**, 1 (2023).
 - [9] T. Christopoulos, E. E. Kriezis, and O. Tsilipakos, Multimode non-Hermitian framework for third harmonic generation in nonlinear photonic systems comprising two-dimensional materials, *Phys. Rev. B* **107**, 035413 (2023).

- [10] A. Gras, W. Yan, and P. Lalanne, Quasinormal-mode analysis of grating spectra at fixed incidence angles, *Opt. Lett.* **44**, 3494 (2019).
- [11] O. Tsilipakos and T. Koschny, Multiresonant metasurfaces for arbitrarily broad bandwidth pulse chirping and dispersion compensation, *Phys. Rev. B* **107**, 165408 (2023).
- [12] P. Lalanne, W. Yan, A. Gras, C. Sauvan, J.-P. Hugonin, M. Besbes, G. Demésy, M. D. Truong, B. Gralak, F. Zolla, A. Nicolet, F. Binkowski, L. Zschiedrich, S. Burger, J. Zimmerling, R. Remis, P. Urbach, H. T. Liu, and T. Weiss, Quasinormal mode solvers for resonators with dispersive materials, *J. Opt. Soc. Am. A* **36**, 686 (2019).
- [13] T. Wu, D. Arrivault, W. Yan, and P. Lalanne, Modal analysis of electromagnetic resonators: User guide for the man program, *Comput. Phys. Commun.* **284**, 108627 (2023).
- [14] T. Christopoulos, O. Tsilipakos, and E. E. Kriezis, Perturbation theory for Kerr nonlinear leaky cavities, *Opt. Lett.* **45**, 6442 (2020).
- [15] W. Yan, R. Faggiani, and P. Lalanne, Rigorous modal analysis of plasmonic nanoresonators, *Phys. Rev. B* **97**, 205422 (2018).
- [16] J. Hu, S. Bandyopadhyay, Y.-H. Liu, and L.-Y. Shao, A review on metasurface: From principle to smart metadevices, *Front. Phys.* **8**, 586087 (2021).
- [17] C. W. Hsu, B. Zhen, A. D. Stone, J. D. Joannopoulos, and M. Soljačić, Bound states in the continuum, *Nat. Rev. Mater.* **1**, 16048 (2016).
- [18] O. Tsilipakos, L. Maiolo, F. Maita, R. Beccherelli, M. Kafesaki, E. E. Kriezis, T. V. Yioultsis, and D. C. Zografopoulos, Experimental demonstration of ultrathin broken-symmetry metasurfaces with controllably sharp resonant response, *Appl. Phys. Lett.* **119**, 231601 (2021).
- [19] C. Sauvan, T. Wu, R. Zarouf, E. A. Muljarov, and P. Lalanne, Normalization, orthogonality and completeness of quasinormal modes of open systems: The case of electromagnetism, *Opt. Express* **30**, 6846 (2022).
- [20] S. Both and T. Weiss, Resonant states and their role in nanophotonics, *Semicond. Sci. Technol.* **37**, 013002 (2022).
- [21] J. D. Joannopoulos, S. G. Johnson, J. N. Winn, and R. D. Meade, *Photonic Crystals: Molding the Flow of Light*, 2nd ed. (Princeton University Press, Princeton, New Jersey, 2008).
- [22] H. Benisty, J.-J. Greffet, and P. Lalanne, *Introduction to Nanophotonics* (Oxford Graduate Texts, Oxford, UK, 2022).
- [23] M. Davanco, Y. Urzhumov, and G. Shvets, The complex Bloch bands of a 2D plasmonic crystal displaying isotropic negative refraction, *Opt. Express* **15**, 9681 (2007).
- [24] M. Nitas, V. Salonikios, and T. V. Yioultsis, Alternative finite element eigenvalue formulations for the simulation of arbitrarily bianisotropic media, *IEEE Trans. Microwave Theory Tech.* **71**, 570 (2023).
- [25] T. Weiss, M. Schäferling, H. Giessen, N. A. Gippius, S. G. Tikhodeev, W. Langbein, and E. A. Muljarov, Analytical normalization of resonant states in photonic crystal slabs and periodic arrays of nanoantennas at oblique incidence, *Phys. Rev. B* **96**, 045129 (2017).
- [26] C. Sauvan, J. P. Hugonin, I. S. Maksymov, and P. Lalanne, Theory of the spontaneous optical emission of nanosize photonic and plasmon resonators, *Phys. Rev. Lett.* **110**, 237401 (2013).
- [27] B. Jin, T. Guo, and C. Argyropoulos, Enhanced third harmonic generation with graphene metasurfaces, *J. Opt.* **19**, 094005 (2017).
- [28] A. Theodosi, O. Tsilipakos, C. M. Soukoulis, E. N. Economou, and M. Kafesaki, 2D-patterned graphene metasurfaces for efficient third harmonic generation at THz frequencies, *Opt. Express* **30**, 460 (2022).
- [29] A. Y. Nikitin, T. Low, and L. Martín-Moreno, Anomalous reflection phase of graphene plasmons and its influence on resonators, *Phys. Rev. B* **90**, 041407(R) (2014).
- [30] E. Hecht, *Optics*, 5th ed. (Pearson Education, Essex, UK, 2015).
- [31] Y. Yang, C. Peng, Y. Liang, Z. Li, and S. Noda, Analytical perspective for bound states in the continuum in photonic crystal slabs, *Phys. Rev. Lett.* **113**, 037401 (2014).
- [32] N. Bernhardt, K. Koshelev, S. J. White, K. W. C. Meng, J. E. Fröch, S. Kim, T. T. Tran, D.-Y. Choi, Y. Kivshar, and A. S. Solntsev, Quasi-BIC resonant enhancement of second-harmonic generation in WS₂ monolayers, *Nano Lett.* **20**, 5309 (2020).
- [33] P. Ren, Z. Huang, S. Luo, J. Liu, X. Dong, H. Zhang, J. Li, and Z. Yang, Quasi-BICs enhanced second harmonic generation from WSe₂ monolayer, *Nanophotonics* **13**, 3449 (2024).
- [34] O. Karni, E. Barré, S. C. Lau, R. Gillen, E. Y. Ma, B. Kim, K. Watanabe, T. Taniguchi, J. Maultzsch, K. Barmak, R. H. Page, and T. F. Heinz, Infrared interlayer exciton emission in MoS₂/WSe₂ heterostructures, *Phys. Rev. Lett.* **123**, 247402 (2019).
- [35] G. Nousios, T. Christopoulos, O. Tsilipakos, and E. E. Kriezis, Integrated lasers with transition-metal-dichalcogenide heterostructures: Analysis and design utilizing coupled-mode theory for two-dimensional materials, *Phys. Rev. Appl.* **19**, 064027 (2023).
- [36] H.-L. Liu, C.-C. Shen, S.-H. Su, C.-L. Hsu, M.-Y. Li, and L.-J. Li, Optical properties of monolayer transition metal dichalcogenides probed by spectroscopic ellipsometry, *Appl. Phys. Lett.* **105**, 201905 (2014).
- [37] C. Hsu, R. Frisenda, R. Schmidt, A. Arora, S. M. Vasconcellos, R. Bratschitsch, H. S. J. van der Zant, and A. Castellanos-Gomez, Thickness-Dependent Refractive Index of 1L, 2L, and 3L MoS₂, MoSe₂, WS₂, and WSe₂, *Adv. Opt. Mater.* **7**, 1900239 (2019).
- [38] T. Wang, D. K. T. Ng, S. K. Ng, Y. T. Toh, A. K. L. Chee, G. F. R. Chen, Q. Wang, and D. T. H. Tan, Supercontinuum generation in bandgap engineered, back-end CMOS compatible silicon rich nitride waveguides, *Laser Photonics Rev.* **9**, 498 (2015).
- [39] M. Besbes and C. Sauvan, Role of static modes in quasinormal modes expansions: When and how to take them into account? *Mathematics* **10**, 3542 (2022).
- [40] M. F. Limonov, M. V. Rybin, A. N. Poddubny, and Y. S. Kivshar, Fano resonances in photonics, *Nat. Photonics* **11**, 543 (2017).
- [41] G. F. Mkrtchian, A. Knorr, and M. Selig, Theory of second-order excitonic nonlinearities in transition metal dichalcogenides, *Phys. Rev. B* **100**, 125401 (2019).